Ocean warming threatens the viability of 60% of Antarctic ice shelves

Clara Burgard, Nicolas Jourdain, Cyrille Mosbeux, Justine Caillet, Pierre Mathiot, Christoph Kittel

Ocean warming threatens the viability of 60% of Antarctic ice shelves

C. Burgard[1,2*], N.C. Jourdain[2], C. Mosbeux[2], J. Caillet[2,3], P. Mathiot[2], C. Kittel[2,4,5]

[1*]Laboratoire d'Océanographie et du Climat: Expérimentations et Approches Numériques (LOCEAN), Sorbonne Université/CNRS/IRD/MNHN, Paris, France.
[2]IGE, Univ. Grenoble Alpes/IRD/CNRS/INRAE/Grenoble INP, Grenoble,France.
[3]Thayer School of Engineering, Dartmouth College, Hanover, NH, USA.
[4]ULiège, Department of Geography, UR SPHERES, Liège, Belgium.
[5]Vrije Universiteit Brussel, Physical Geography Research Group, Department of Geography, Brussels,Belgium.

*Corresponding author(s). E-mail(s): clara.burgard@locean.ipsl.fr;

Abstract

The disappearance of ice shelves, the floating margins of the Antarctic ice sheet that restrain the ice flow into the ocean [1–3], would strongly accelerate the Antarctic contribution to sea-level rise [4–6]. Their viability in a warming world has motivated a lot of work, strongly focussing on the influence of the warming atmosphere [7–10]. Here we revisit the concept of ice-shelf viability in a holistic manner, taking into account mass loss due to both the atmosphere and the ocean to estimate when it becomes virtually impossible for the ice shelves to maintain their present-day shape. We show that, for a scenario remaining largely below 2°C of global warming, only one out of 64 ice shelves likely becomes non-viable by 2300. For a scenario reaching nearly 12°C of global warming by 2300, many ice shelves become non-viable once global warming exceeds 4.5°C, mainly due to an increase in ocean-induced melt. 26 ice shelves are likely non-viable by 2150, and 38 in 2300. Ice-sheet regions restrained by these 38 ice shelves represent a

sea-level rise potential of 10 m. Our estimates are latest bounds for reaching non-viability and ice-shelf collapse could occur even earlier, in particular due to the synergy with hydrofracturing.

Keywords: Antarctica, Climate change, Ice shelves, Modeling

The Antarctic ice sheet has been losing mass at an accelerating pace, becoming a significant contributor to global sea-level rise [4]. Ice shelves, the floating margins of the Antarctic ice sheet, are a crucial element controlling this mass loss. As they restrain the ice flow from the grounded ice sheet to the ocean through so-called *buttressing* [1, 2], they represent a safety band around Antarctica [3]. Their thinning and eventual collapse hence accelerates the ice discharge into the ocean [5, 6] and could, in addition, trigger two instability mechanisms that accelerate Antarctic mass loss: the Marine Ice Sheet Instability (MISI) [11, 12] and the Marine Ice Cliff Instability (MICI) [13, 14]. Projections assuming both instabilities to take place in the 21st century result in a global sea-level rise of up to 1.75 m until 2100 [4], threatening coastal regions all over the world.

Ice shelves subsist due to a fragile balance between mass gain and mass loss at their boundaries with the grounded ice sheet, the atmosphere, and the ocean. Over the past decades, when considering all of Antarctica, mass loss to the ocean through iceberg calving and ice-shelf basal melting has substantially compensated the large mass gain through the ice flow from the grounded ice sheet to the ice shelf and the minor mass gain through the atmosphere [15]. Lately, especially in the Amundsen Sea, many ice shelves have been out of balance, significantly losing mass [15, 16].

As anthropogenic climate change further unfolds, more and more pressure will be exerted on the ice shelves, both at their surface due to a warmer atmosphere [17, 18], and at their base due to more intrusions of warm water [19, 20], leading to ice-shelf thinning and retreat. At the same time, the thinning of an ice shelf usually reduces buttressing, leading to a faster ice flow from the grounded ice sheet to the ice shelf [12],

which tends to make the ice shelf thicker. The competing evolution of such processes will drive the evolution of ice shelves and their potential disappearance in the next decades to centuries. Here, we examine if, when, and why ice shelves will no longer be viable, at the latest, due to changes in atmosphere and ocean conditions.

Estimating non-viability

The idea of a climatic limit of viability for ice shelves has been explored since the 1960s, based on the observation that temperate ice shelves (close to their freezing temperature) do not exist and that the warmest parts of the Antarctic Peninsula, as well as most parts of Greenland, are free of ice shelves [7, 8]. A limit based on an air-temperature threshold was suggested and further refined when several ice shelves of the Antarctic Peninsula retreated in the late 1990s and early 2000s [9, 10]. The collapse of Larsen A-B in 1995 and Larsen B in 2002 highlighted the importance of hydrofracturing [21–23] for the viability of ice shelves. Hydrofracturing occurs when surface meltwater favors the propagation of crevasses and eventual disintegration of the ice shelf. However, hydrofracturing can only take place if the ice shelf is sufficiently weak [24]. Ice-shelf thinning due to changes in ocean or atmosphere conditions can provide the necessary mechanical preconditioning [25–27].

The progressive fragmentation of Thwaites glacier's western tongue from approximately 2009 [28] showed that an ice-shelf collapse can even occur in the absence of surface meltwater [29, 30]. It was driven by a combination of ocean-induced ice-shelf thinning [31, 32] and increased ice damage [33]. These elements prove that the limit of viability for ice shelves cannot be defined solely from air temperature or surface melt rates.

We therefore revisit the concept of ice-shelf viability in a holistic approach, including all terms contributing to the Antarctic ice-shelf mass balance (Fig. 1): the flux

from the grounded ice sheet to the floating ice shelf (called grounding-line flux hereafter), the iceberg calving flux at the ice-shelf front, the surface mass balance (the difference between surface accumulation and ablation), and the basal mass balance (the difference between basal melting and refreezing). We define the limit of viability as the moment where mass loss at the surface, at the base, and at the front exceeds the maximum possible incoming grounding-line flux. This is done for the individual ice shelves and under different greenhouse gas emission scenarios. The maximum possible grounding-line flux corresponds to the flux in the absence of ice-shelf buttressing, i.e. the flux that would occur immediately after an abrupt ice-shelf collapse with maximal damage. We use it so that we do not have to rely on the transient evolution of ice-sheet models in which ice-shelf calving and damage are either poorly or not represented [34]. Our limit of viability thus represents the ocean and atmosphere conditions for which it is virtually impossible that an ice shelf maintains its current shape in the long term, as it loses more mass than it gains, and does not represent the actual date at which an ice shelf disintegrates or reaches zero thickness. As evolving calving and damage cannot explicitly be represented, our approach provides the latest-bound conditions in which an ice shelf will initiate long-term thinning due to the imbalance between mass gain and mass loss. Depending on the initial shape of the ice shelf and the magnitude of the imbalance. This thinning may mechanically weaken the ice shelf, making it more vulnerable to disintegration, or may lead to a retreat into a different equilibrium with a reduced extent.

We derive mass loss and gain at the interface with ocean and atmosphere based on a range of climate simulations [35] covering 1850 to 2300 under two future-emission scenarios. In the low-emission scenario, global warming remains below 2°C until 2300. In the high-emission scenario, global warming reaches nearly 12°C by 2300. On the atmospheric side, we use regional climate model simulations [17, 36] of the surface mass balance driven by the global climate simulations. On the oceanic side, we derive

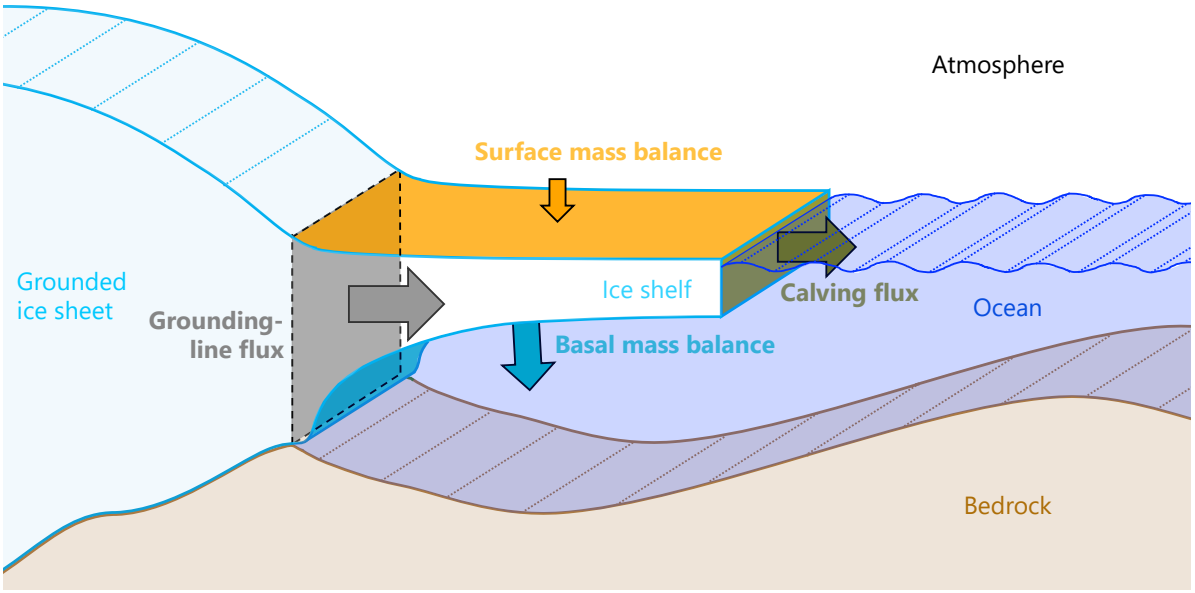

Fig. 1 Schematic of the terms contributing to the Antarctic ice-shelf mass balance. Due to ice dynamics, mass is gained through the grounding-line flux (the ice flow from the grounded ice sheet to the floating ice shelf) and lost through the calving of icebergs at the ice-shelf front. The surface mass balance, which describes mass exchange with the atmosphere, is determined by the difference between accumulation (mainly snowfall, but also rainfall and frost deposition) and ablation (runoff and sublimation). The basal mass balance, which describes mass exchange with the ocean, is determined by the difference between basal melting and refreezing.

the basal mass balance from the climate simulations using a range of parameterisations based on either simple physics [37] or artificial neural networks [38]. On the ice dynamics side, we estimate the maximal grounding-line flux by simulating the instantaneous response of the current ice sheet to a total loss of ice-shelf buttressing: using an ice-sheet model in a state constrained by observations, we remove all ice shelves at once. We repeat the experiment with three different bed plasticities to take into account uncertainty arising from ice-sheet model assumptions. As large uncertainties around future calving evolution remain [39, 40], we assume the lowest bound by setting calving to zero. Finally, to constrain our analysis to a plausible ensemble for every ice shelf, we weigh the multiple combinations of climate models, basal melt

parameterisations, and bed plasticities based on (1) their comparison to the observed ice-shelf mass balance [15] and (2) the plausibility of the models' equilibrium climate sensitivity [36]. More details are provided in the Methods section.

Our approach relies on the current ice-sheet geometry. However, repeating the analysis for two different plausible future ice-sheet geometries shows that our conclusions remain on the conservative side, even though grounding-line retreat and increased precipitation over the grounded ice sheet locally lead to an increase in the grounding-line flux and its upper estimate (more details in the Methods section).

Reaching non-viability

The time of reaching non-viability strongly depends on the scenario (Fig. 2). While only one of the 64 ice shelves becomes likely non-viable by 2300 in the low-emission scenario, 26 become likely non-viable before 2150 in the high-emission scenario, a number that raises to 38 out of 64 by 2300. There is very high confidence on the widespread non-viability in the high-emission scenario, with 30 very likely non-viable ice shelves by 2300.

Looking at the projections for the low-emission scenario, the likelihood of non-viability remains nearly unchanged from present-day to the mid 23$^{\text{rd}}$ century. The number of ice shelves crossing the 10% and 33% likelihood of becoming non-viable increases more rapidly after 2250 (Fig. 2a), and one ice shelf becomes likely non-viable shortly before 2300. This hints at possible long-term changes in viability beyond 2300, despite a clear emission reduction and global air temperature stabilisation after 2100.

In the high-emission scenario, a majority of ice shelves gradually moves towards non-viability between 2050 and 2300. The period between approximately 2085 and 2170 marks the period with the highest rate of ice shelves reaching likely non-viability, with 44% of the ice shelves becoming likely non-viable and 30% even very likely, over 85 years. Looking at the global surface air temperature evolution as a proxy for climate

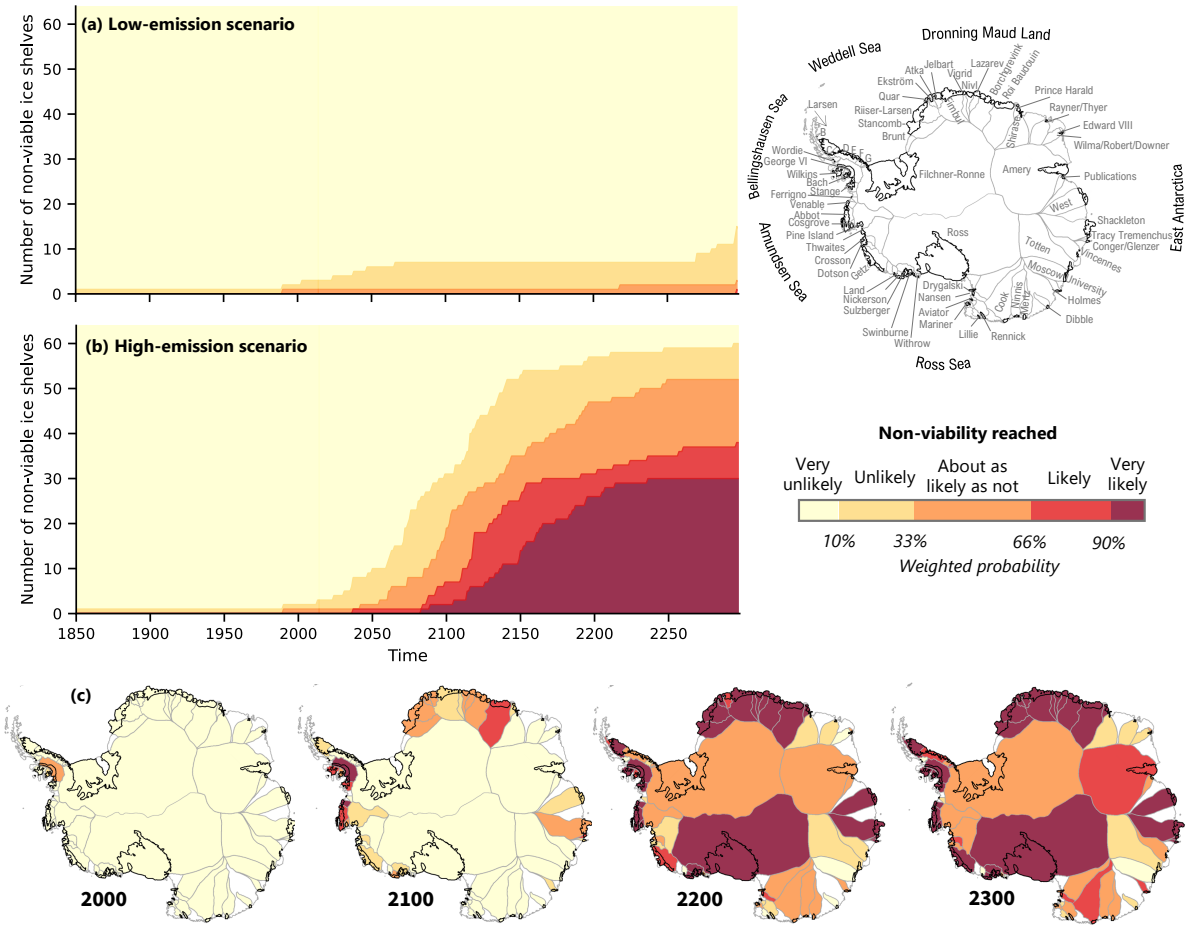

Fig. 2 Distribution of ice-shelf non-viability likelihood over time and space. Evolution of the number of non-viable ice shelves over time for (a) the low-emission scenario and (b) the high-emission scenario over time. (c) Spatial distribution of the weighted likelihood of reaching non-viability for the years 2000, 2100, 2200 and 2300 in the high-emission scenario. The color corresponding to the likelihood is applied to the ice shelves and their associated drainage basins for more visibility. Geographical indications of the main Antarctic regions, ice shelves (black contours) and associated drainage basins (grey contours) are shown in the upper right corner. Drainage basins in white are not considered because their are associated to no or a very small ice shelf.

change (Fig. 3), this corresponds to crossing a threshold of ∼4.5°C of global warming compared to the early historical period (1850-1900).

This effect is widespread and not confined to a given region. Ice shelves become likely and very likely non-viable between 2100 and 2300 all around Antarctica

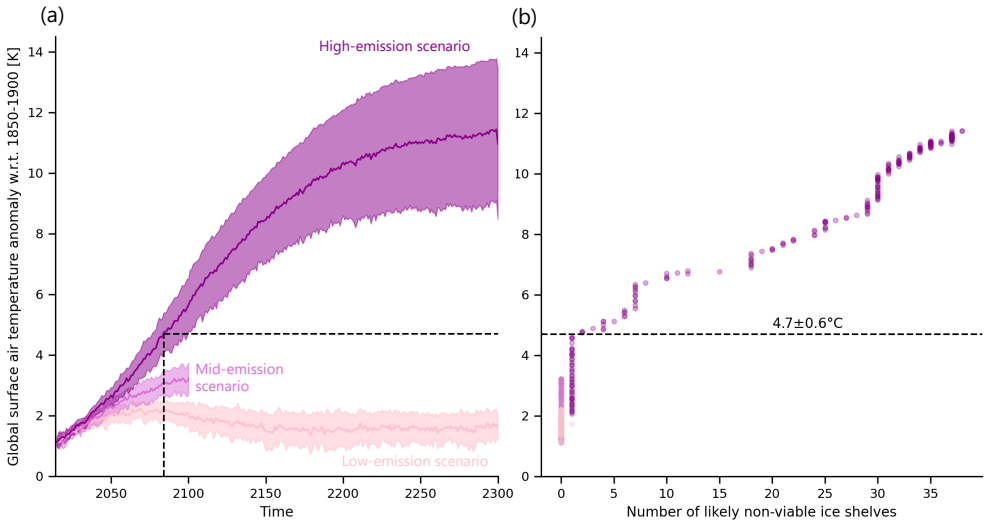

Fig. 3 Link between global warming and number of ice shelves reaching likely non-viability. (a) Weighted average (line) and standard deviation (shading) of the global surface air warming across climate models with regard to the 1850-1990 average for the three emission scenarios. (b) Number of likely non-viable ice shelves as a function of the average global surface warming. The dotted line highlights the warming in 2084, the date from which the rate of ice shelves becoming non-viable increases rapidly.

(Fig. 2c). The main hot spots are West Antarctica, where a majority of ice shelves from the Bellingshausen Sea to the Ross Sea are likely or very likely non-viable by 2200, as well as the ice shelves from the Eastern Weddell Sea to the eastern edge of Dronning Maud Land. A few other ice shelves in East Antarctica, such as West and Shackleton ice shelves, also display a very high likelihood of becoming non-viable.

About 40% of the area covered by drainage basins feeding likely non-viable ice shelves in 2300 is resting on bedrock that has been pressed below sea level due to the weight of accumulating ice mass over thousands of years. Such low bedrock is one of the necessary conditions for the marine ice sheet and ice cliff instabilities, which both could trigger rapid mass loss episodes from the ice sheet to the ocean [11–14]. Likely non-viability of the associated ice shelves thus represents a theoretical potential for ∼10 m of long-term sea-level rise, when aggregating the volume above flotation of these basins and assuming the total loss of buttressing due to a complete disappearance

of the associated ice shelves. This is an upper estimate as the occurrence of these instabilities also depends on other factors, notably the gradient of the bed slope [12] or the presence of high cliffs [41], or the potentially persisting buttressing effect due to the reduced remains of a non-viable ice shelf.

Drivers of non-viability

The link between the rate of ice shelves becoming non-viable and the rate of global warming could support the hypothesis that the viability of ice shelves is directly linked to an atmospheric temperature threshold [9, 10, 42]. However, global atmospheric warming is only one of multiple symptoms of climate change, other ones being for example ocean warming and changes in the ocean circulation. Using our holistic perspective, we investigate more thoroughly the mechanisms triggering non-viability. This is done for every member of our ensemble, by quantifying the relative contribution of each mass flux to the ice-shelf mass loss at the date when non-viability is reached.

The ocean is by far the main driver for reaching non-viability (Fig. 4) and the surface mass balance has a much smaller influence. In both scenarios, basal melting explains more than half of the mass loss needed to reach non-viability for all ice shelves that reach non-viability. For the high-emission scenario, this is not surprising as a steep increase in basal melting starts around 2100 (Extended Data Fig. 3). Nevertheless, we could not pinpoint a given ocean temperature threshold for non-viability.

The surface mass balance has a lower influence on non-viability. In the low-emission scenario, the surface mass balance does not lead to mass loss in any ice shelf at the moment of reaching non-viability and rather counteracts mass loss by 15% on average, confirming that an increase in accumulation prevails [17]. In the high-emission scenario, the surface mass balance leads to mass loss at the moment of reaching

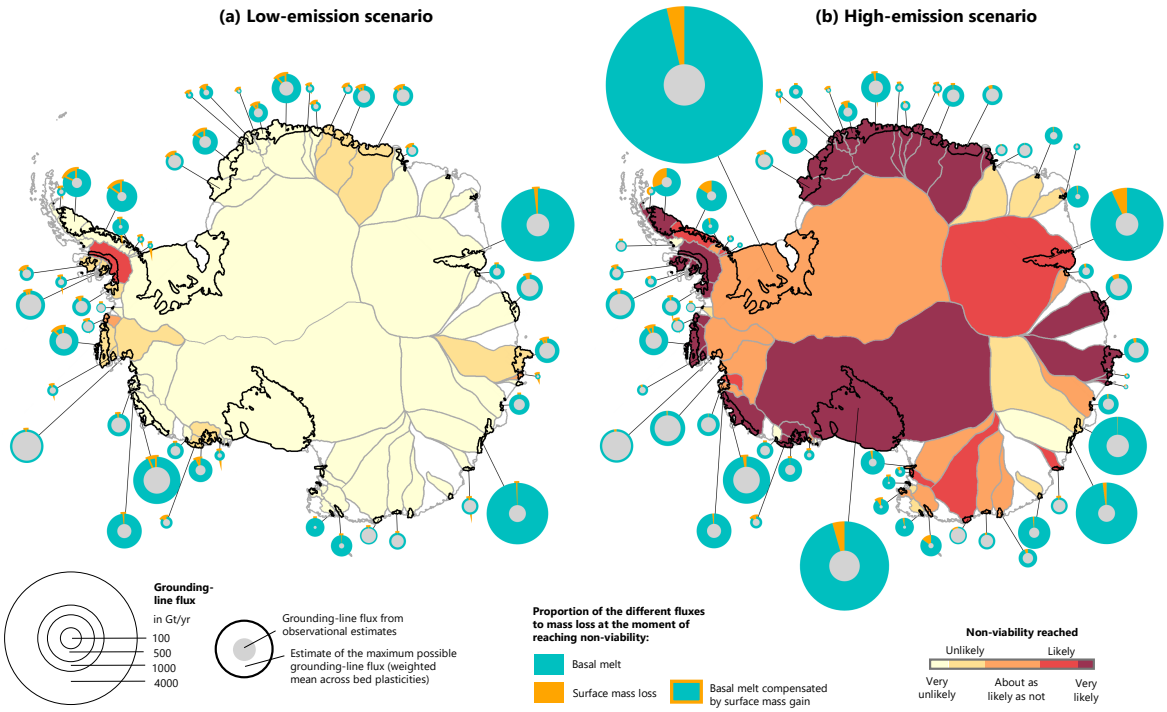

Fig. 4 Relative importance of the different mass fluxes to reaching non-viability. Average ratio between basal melt (blue) and surface mass balance (orange), respectively, and the maximal grounding-line flux at the moment when non-viability is reached for (a) the low-emission scenario and (b) the high-emission scenario. Circles are only shown if at least one ensemble member reaches non-viability before 2300. The grey circle represents the reference grounding-line flux and the area of the pie chart represents the upper-grounding line flux estimate (represented by a weighted mean of the estimates across bed plasticities). The color corresponding to the likelihood of non-viability in 2300 is applied to the ice shelves and their associated drainage basins for more visibility.

non-viability for 60% of the ice shelves, but contributing on average only 2.5% to non-viability for these ice shelves, with a maximum at 50% for the remains of Larsen B.

Zooming in on the main hot-spot regions of current high basal melt, most of them being prone to marine ice-sheet instability (Pine Island and Thwaites ice shelves in the Amundsen Sea and Totten and Moscow University ice shelves in East Antarctica), none of them is likely non-viable by 2300. The probability is higher for Pine Island and Thwaites ice shelves (about as likely as not), where the upper estimate for the grounding-line flux is only slightly higher than the present flux, while Totten and Moscow University need a large increase in mass loss to reach non-viability. On the

one hand, this is somehow consistent with the mechanism of marine ice-sheet instability: the weakening of an ice shelf increases the grounding-line flux, which decreases the mass of the grounded ice sheet but brings more mass to the ice shelf. This means, maybe counter-intuitively, that a marine ice-sheet instability would support the viability of an ice shelf, at least for some time, as long as there remains substantial amounts of grounded ice upstream. On the other hand, we emphasise that our approach results in a latest bound for non-viability and does not rule out an actual collapse occurring earlier, for example through long-term thinning or through hydrofracturing or damage and rifting, as suggested e.g. for some parts of Thwaites ice shelf [43, 44].

Implications

Our results show that current choices to change emission pathways could significantly impact the likelihood of long-term loss of most Antarctic ice shelves. The viability of ice shelves strongly depends on the emission scenario, as only one ice shelf becomes likely or very likely non-viable by 2300 in the low-emission scenario versus 59% in the high-emission scenario. This difference between scenarios is particularly visible after 2085, due to basal melting substantially increasing across all ice shelves around this date in the high-emission scenario (Extended Data Fig. 3-4). Nevertheless, this does not mean that the emission pathway leading to 2085 is not relevant to ice-shelf viability, as increased basal melting is likely a lagged response to global atmospheric warming and therefore a consequence of emissions happening already earlier in the century (Fig. 3.

Our viability limit suggests that, in terms of balance between mass gain and mass loss, 40% of the ice shelves at least as likely as not remain stable under extreme conditions. This might appear a surprisingly large fraction and suggest that ice shelves are quite robust considering only the mass balance. However, this estimate is on the most conservative side and actual thinning, retreat, or collapse could occur even

sooner, depending on the vulnerability of a given ice shelf to other processes such as damage, rifting, hydrofracturing or calving. Our definition of non-viability represents the latest limit for viability as it is bound by an extreme mass gain from the ice sheet and minimal mass loss from calving. However, mass gain through the grounding-line flux will not necessarily reach its upper limit, which inherently integrates the effect of damage, rifting and hydrofracturing. Also, mass loss through calving is projected to increase in the future for mid- and high-emission scenarios [39, 40]. Further, feedbacks between basal melting and ice geometry [45] or between calving and basal melting [46] could affect the stability of the ice shelf and potentially slightly alter the conditions to reach non-viability.

We emphasise that our non-viability estimate does not correspond to the most likely timing of collapse and rather to an upper bound of the time when ice-shelf shrinking becomes inevitable. The rate of long-term shrinking, the magnitude of buttressing loss, and the timing of eventual disappearance after reaching non-viability largely differs between ice shelves as it depends on the ice-shelf shape and on the imbalance between mass gain and mass loss. Nevertheless, in most cases, ocean-induced melt continues to increase after reaching the viability limit in the high-emission scenario (Extended Data Fig. 2), suggesting that the rate of thinning could further accelerate beyond this limit and thus accelerate ice-shelf shrinking in all cases. In addition, the occurrence of other processes, such as increasing damage, hydrofracturing or stronger calving rate, could lead to an actual collapse before a complete thinning-induced disappearance. Modelling tools are not ready yet for accurately simulating the prognostic interplay between these processes over multiple centuries, but we are confident that an upper bound can be estimated using our approach.

Our non-viability estimate can nonetheless be used as a proxy for the prior ice-shelf mechanical weakening required for hydrofracturing [25–27]. This can be compared to the estimates of surface hydrological conditions also required for hydrofracturing:

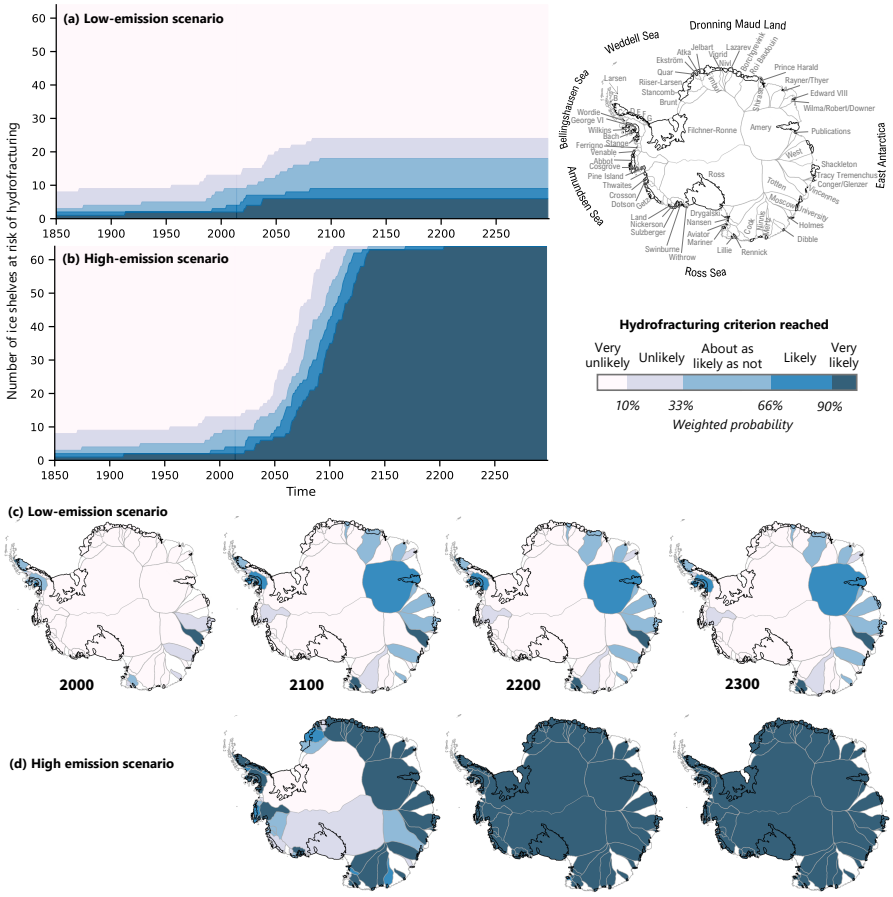

Fig. 5 Distribution of the hydrofracturing risk over time and space, based on the presence of liquid water beyond firn saturation. Evolution of the risk of hydrofracturing using the method introduced by Jourdain et al. [36] for (a) the low-emission scenario and (b) the high-emission scenario over time. Spatial distribution of the weighted likelihood of the risk of hydrofracturing for the years 2000, 2100, 2200 and 2300 in the (c) low- and (d) high-emission scenario. The color corresponding to the likelihood is applied to the ice shelves and their associated drainage basins for more visibility. Geographical indications of the main Antarctic regions, ice shelves (black contours) and associated drainage basins (grey contours) are shown in the upper right corner. Drainage basins in white are not considered because their are associated to no or very small ice shelves. The probabilities are calculated for the seven CMIP6 models and their respective weights, and the thresholds are sampled in a normal distribution that is at 90% between 50 and 250 $\mathrm{kg\,m^{-2}\,yr^{-1}}$ [36].

the production of liquid water beyond firn saturation, as estimated in Jourdain et al. [36]. Following their method, the surface hydrological conditions become prone to hydrofracturing before non-viability is reached for all ice shelves (Fig. 5), indicating

that ice shelves that weaken beyond non viability will likely quickly be exposed to hydrofracturing, and hence to an actual collapse.

On another aspect, our study further underlines the importance of the ocean for the present and future evolution of the Antarctic ice sheet. However, global climate models currently struggle to simulate accurate Southern Ocean properties [47, 48]. Reducing biases in the simulation of the Southern Ocean in global climate models, e.g. by improving the representation of processes on the continental shelf or by including ice-ocean interactions more systematically [49], is therefore crucial. This should be a priority of the climate research community to better apprehend future sea-level evolution and the effect of meltwater on the oceanic circulation.

Finally, our results show that the risk of non-viability is a circum-Antarctic problem, suggesting it to be a consequence of global temperature and circulation changes, rather than local changes. The likelihood of reaching non-viability is not tightly linked to one region as most ice shelves in the Bellingshausen, Amundsen and Ross seas, as well as in Dronning Maud Land, but also a few large ice shelves in East Antarctica are at risk of becoming non-viable. The impact of the potential long-term ice-shelf loss is strong in particular in the Bellingshausen, Amundsen and Ross seas. There, most of the associated drainage basins rest on bedrock below sea level and have a sea-level rise potential of several meters on the long term [50].

Methods

Topography and boundaries of individual ice shelves

The boundaries used to define the 64 largest ice shelves of Antarctica are the ones used in the Ice sheet Mass Balance Intercomparison Exercise (IMBIE) [51]. The ice topography is taken from BedMachine-Antarctica, version 2 [52]. All datasets are regridded to a 4-km stereographic grid to limit computational cost. This resolution is a reasonable compromise to represent the different components while keeping a balance

between too high or too low confidence in the chosen resolution of the processes. For example, the grounding-line flux is inferred from the ice-sheet Elmer/Ice model at the kilometer-scale, the basal melt parameterisations were calibrated on ocean simulations at 5-8 km resolution, and the surface mass balance was downscaled from 35 km output. To minimise grounding-line imprecisions, we work with an "ice-shelf concentration", which describes the fraction of a cell covered by ice-shelf parts. This allows us to better account for points near the grounding line than if we would only consider cells completely covered by ice shelves.

Forcing

The ocean and atmosphere forcing are based on the outputs from seven models from the sixth phase of the Coupled Model Intercomparison Project (CMIP6 [35]) covering 1850 to 2300, under the Shared Socio-economic Pathways SSP1-2.6 (low-emission scenario) and SSP5-8.5 (high-emission scenario) that diverge from the historical period in 2015: ACCESS-CM2, ACCESS-ESM1-5, CESM2-WACCM, CanESM5, IPSL-CM6A-LR, MRI-ESM2-0, UKESM1-0-LL. For completeness, we also investigated six additional models (CESM2, CNRM-CM6-1, CNRM-ESM2-1, GFDL-CM4, GFDL-ESM4, MPI-ESM1-2-HR) and the mid-emission scenario SSP2-4.5, which were only run until 2100 (Extended Data Fig. 5). Conclusions until 2100 remain robust using the larger model ensemble.

Ice-shelf mass balance

Our results are based on the analysis of the different contributors to the ice-shelf mass balance: the basal mass balance, the surface mass balance, the calving flux and the grounding-line flux (Extended Data Fig. 1 to 4). If the ice-shelf mass balance becomes negative and remains negative until 2300, non-viability is reached.

Basal mass balance

Ocean-induced sub-shelf melt and refreezing are computed by applying basal melt parameterisations to geometrical properties of the sub-shelf cavities and to ocean temperature and salinity profiles inferred from yearly climate model output in front of the different ice shelves. To prepare these profiles, we first interpolate the coarse climate model output to a 8 km stereographic grid and extrapolate properties horizontally from contiguous ocean points to the points not covered by the CMIP6 model grid [53]. We then horizontally average the continental shelf (bathymetry shallower than 1500 m) ocean properties within 50 km of the ice-shelf front to obtain a single potential temperature profile and a single practical salinity profile in front of each ice shelf, like in Burgard et al. [37].

Directly taking the ocean properties from the CMIP6 models leads to very large biases in estimated melt rates, sometimes of the order of several hundreds of $\mathrm{Gt\,yr^{-1}}$, which would strongly affect projected melt rates. Instead, we correct the CMIP6 temperature and salinity profiles of individual ice shelves by subtracting the simulated 1997–2014 average and adding a present-day estimate constrained by observations: either the climatology proposed for the Ice-Sheet Model Intercomparison Project for CMIP6 (ISMIP6) [54], or the output from a present-day ocean model hindcast forced by an atmospheric reanalysis [20]. We use these two different present-day estimates because some regions, such as Dronning Maud Land or the southwestern Weddell Sea, are not well covered by observations and the interpolated values given in the ISMIP6 climatology are thus not necessarily reliable. For every ice shelf, we compute the difference between the observational sub-shelf melt estimates [15] and the melt inferred based on CMIP6 ocean properties corrected with the observational climatology on the one hand, and corrected with the model hindcast on the other hand. We select the correction where the median of this difference is lowest. The resulting choices are:

- *ISMIP6 climatology*: Filchner-Ronne, Rayner/Thyer, Amery, Publications, West, Shackleton, Tracy Tremenchus, Conger/Glenzer, Vincennes Bay, Totten, Moscow University, Dibble, Mertz, Ninnis, Cook, Rennick, Lillie, Mariner, Aviator, Drygalski, Ross, Withrow, Swinburne, Sulzberger, Getz, Crosson, Dotson, Thwaites, Pine Island, Cosgrove, Larsen E
- *Ocean-model present-day hindcast*: Stancomb Brunt, Riiser-Larsen, Quar, Ekström, Atka, Jelbart, Fimbul, Vigrid, Nivl, Lazarev, Borchgrevink, Roi Baudouin, Prince Harald, Shirase, Edward VIII, Wilma/Robert/Downer, Holmes, Nansen, Nickerson, Land, Abbot, Venable, Ferrigno, Stange, Bach, Wilkins, George VI, Wordie, Larsen B, Larsen C, Larsen D, Larsen F, Larsen G

We use these corrected ocean profiles as input for six different basal melt parameterisations: (1) the linear-local parameterisation [55], (2) the quadratic-local parameterisation using a constant Antarctic slope [13, 37, 56], (3) the quadratic-local parameterisation using a local slope [37, 57, 58], (4) the plume parameterisation [59, 60], (5) the box parameterisation [61], and (6) the neural-network parameterisation introduced in Burgard et al. [38]. The physics-based parameterisations (1) to (5) are implemented as described in Burgard et al. [37], except a modified method to infer the depth of the plume origin.

The linear parameterisation is formulated as follows [37]:

$$m = \gamma_{TS} \times \frac{c_{\mathrm{oc}}}{L_i} \frac{\rho_{\mathrm{oc}}}{\rho_{\mathrm{i}}} (T_{\mathrm{oc}} - T_{\mathrm{f,\,oc}}) \tag{1}$$

where c_{oc} is the specific heat capacity of the seawater (3974 J kg^{-1}), ρ_{oc} and ρ_i are, respectively, the density of the seawater (1028 kg m^{-3}) and the ice (917 kg m^{-3}), T_{oc} and S_{oc} are the temperature and salinity averaged over a boundary layer below the ice shelf, T_f is the freezing point, L_i is the latent heat of fusion (3.34×10^5 J kg^{-1}).

with the freezing temperature:

$$T_{\mathrm{f,\ oc}} = \lambda_1 S_{\mathrm{oc}} + \lambda_2 + \lambda_3 z_{\mathrm{draft}} \tag{2}$$

λ_1, λ_2 and λ_3 are the coefficients for the freezing point equation (λ_1 = -5.75 $\times$ 10^{-2} °C PSU^{-1}, λ_2 = 8.32 $\times$ 10^{-2} °C, λ_3 = 7.59 $\times$ 10^{-4} °C m^{-1}), z_{draft} is the depth of the ice-shelf draft (negative below sea level). γ_{TS} is the turbulent exchange velocity, assuming a constant current speed U_{Ant} around Antarctica, and is the calibration parameter.

The quadratic parameterisation is formulated as follows [37]:

$$m = K \sin\theta \times \frac{\rho_{\mathrm{oc}}}{\rho_{\mathrm{i}}} \left(\frac{c_{\mathrm{oc}}}{L_i} \right)^2 \beta_S S_{\mathrm{oc}} \frac{g}{2 \mid f \mid} \mid T_{\mathrm{oc}} - T_{\mathrm{f,\ oc}} \mid (T_{\mathrm{oc}} - T_{\mathrm{f,\ oc}}) \tag{3}$$

where g is gravity (9.81 m s^{-2}), f is the Coriolis parameter (-1.4 $\times$ 10^{-4} s^{-1}), and β_S is the salt contraction coefficient (7.86 $\times$ 10^{-4} PSU^{-1}). K is the parameter to calibrate.

Due to very large biases, we decided to calibrate Filchner-Ronne and Ross ice shelves separately from the other ice shelves for the linear and quadratic parameterisations. For the *Antarctic* slope formulation, we assume a uniform slope $\sin\theta_{\mathrm{Ant}}$ = 6.9$\times$$10^{-3}$. In the *local* slope formulation, we estimate the local slope θ_{loc} between the neighbouring grid cells in x- and y- directions at each ice-shelf point.

The formulations of the box and plume model are more complex and we refer to their description in Burgard et al. [37], based on the original formulations from Reese at al. [61] and Lazeroms et al. [59, 60] respectively. For the box model, we use the number-of-box criterion used for PICO. For the plume parameterisation, we use a new method to infer the grounding-line depth representing the plume origin, like in

Lambert and Burgard (2025) [62]. Instead of exploring all directions for each point, we propagate the plume path from each grounding-line point to the rest of the ice shelf.

All of these parameterisations depend on one or two calibration parameters. Due to the low number of matching observational estimates of ocean properties and sub-shelf melt, we use cavity-resolving ocean simulations produced with the NEMO ocean model (Nucleus for European Modelling of the Ocean [63]) at 0.25° of resolution for the calibration (i.e. a resolution of 8 km in both directions at 70° S), as in previous studies [37, 38]. To reduce the calibration uncertainty, we calibrate the parameterisations using simulations covering both present-like and warmer ocean conditions. In addition to the ensemble of four present-day global simulations used for calibration in Burgard et al. [37, 38], we use a global 70-year ocean simulation in conditions plausible by the late 23$^{\text{rd}}$ century in the SSP5-8.5 scenario [20], and three additional new circum-Antarctic simulations: a hindcast over 1982–2014 (driven by the reanalysis JRA55-do [64], 5-day outputs from eORCA025.L121 [20], monthly runoff from MAR [17], and fixed annual calving rates from Rignot et al. [65]) and two projections over 2014–2100 under the SSP5-8.5 scenario (adding a 30-year rolling anomaly for each month for the atmosphere, ocean, surface runoff inferred from CNRM-CM6-1 and MAR projections [17] to the present-day forcing fields from 1982 to 2013 until 2100). The two latter projections differ by the choice of including the runoff from the ice-sheet surface in one and not in the other.

For evaluation of these additional simulations, we provide a comparison of the circum-Antarctic configuration with the global NEMO simulation (Extended Data Fig. 9). We refer to Mathiot and Jourdain [20] for the exhaustive evaluation of the global NEMO simulation, considered as the reference for this evaluation (especially for the temperature in front of the ice shelves). Both NEMO configurations produce melt estimates close to observations although they tend to underestimate the total basal melt. The regional configuration, like its parent configuration, correctly represents

the temperature in the cold cavities (Ross and Filchner-Ronne), resulting in correct melt rates. Similarly, they both correctly represent the advection of Circumpolar Deep Water into the Amundsen Sea. Finally, the regional configuration simulates slightly lower iceberg melt (-125 $\mathrm{Gt\,yr^{-1}}$) and less variability. This can be explained by the fact that some of the icebergs leave the domain of the regional configuration at its northern boundary without melting.

For the physics-based parameterisations (1) to (5), we calibrate the parameter(s) to obtain the minimal root-mean-squared-error of the integrated ice-shelf melt across time and ice shelves (same method as Burgard et al. [37]). The resulting parameters are the following (LARGE being used for Filchner-Ronne and Ross ice shelves, SMALL being used for the others):

- For the linear parameterisation: $\gamma_{\mathrm{TS,SMALL}} = 10.6{\times}10^{-6}\ \mathrm{m\,s^{-1}}$ and $\gamma_{\mathrm{TS,\ LARGE}} = 2.8{\times}10^{-6}\ \mathrm{m\,s^{-1}}$
- For the quadratic parameterisation assuming a constant Antarctic slope: $K_{\mathrm{SMALL}} = 4.7{\times}10^{-5}$ and $K_{\mathrm{LARGE}} = 1.1{\times}10^{-5}$
- For the quadratic parameterisation using the local slope: $K_{\mathrm{SMALL}} = 7.1{\times}10^{-5}$ and $K_{\mathrm{LARGE}} = 3.2{\times}10^{-5}$
- For the box parameterisation: $\gamma_T^\star = 0.88{\times}10^{-5}\ \mathrm{m\,s^{-1}}$ and $C = 2.9{\times}10^{6}\ \mathrm{m^6\,s^{-1}\,kg^{-1}}$
- For the plume parameterisation: $C_d^{1/2}\Gamma_{TS} = 9.3{\times}10^{-4}$ and $E_0 = 3.0{\times}10^{-2}$

For the neural network, we calibrate the parameters to obtain the minimal root-mean-squared-error of the melt on the grid-cell level over time and space (same method as Burgard et al. [38]).

Surface mass balance

To estimate the atmospheric term contributing to the ice-shelf mass balance, we compute the Surface Mass Balance (SMB) as the difference between accumulation and ablation of mass at the surface. We do not directly use the SMB from the climate

models because their overly low resolution is not sufficient to represent the topography of Antarctic ice shelves and because they usually do not represent the polar physical processes needed to simulate the SMB evolution. Instead, we rely on regional projections performed with the hydrostatic atmospheric model MAR (*Modèle Atmosphérique Régional* [66]) forced by several climate models and emission scenarios. We refer to Kittel et al. [17] for exhaustive details on the model configuration used. The MAR simulations are forced by the climate models IPSL-CM6A-LR (1980–2014 historical and 2015–2300 for the SSP5-8.5 scenario) and UKESM1-0-LL (1980–2014 historical and 2015–2100 for both SSP1-2.6 and SSP5-8.5 scenarios). More MAR simulations are available for three of the six additional CMIP6 models used until 2100 (Extended Data Fig. 5), from 1980 to 2100: CESM2 and MPI-ESM1-2-HR for the historical, SSP1-2.6, SSP2-4.5 andd SSP5-8.5 scenarios, and CNRM-CM6-1 for the historical and SSP5-8.5 scenario. For the other CMIP6 models, scenarios, or periods not covered by the MAR simulations, we use the SMB emulation trained with the aforementioned MAR simulations, as described and evaluated in Jourdain et al. [36]. These emulations are based on the changes in yearly surface air temperatures, as simulated in the corresponding CMIP6 simulations, and on physical and statistical relationships.

Rainfall, sublimation and deposition are taken into account in the SMB simulated by MAR as it accounts for the difference between accumulation (snowfall, liquid precipitation, and deposition) and ablation (runoff and sublimation). The emulation method, however, is applied to CMIP simulations not downscaled with MAR and assumes that rainfall plays a negligible role in generating runoff compared to surface melt [30, 36]. This assumption is supported by the extended MAR simulation under the highest emission scenario, which shows that rainfall remains a minor component of liquid production across all ice shelves until 2100, contributes less than 10% by 2200, and becomes significant only locally by 2300—after most ice shelves have surpassed their viability thresholds. As such, omitting rainfall leads to a conservative

estimate of ice shelf non-viability, consistent with our treatment of other fluxes. Similarly, sublimation and deposition are neglected in the emulation method, as they are not expected to substantially affect future mass balance [17].

Although the MAR resolution of 35 km represents a significant improvement compared to the resolution of climate models, this resolution is still not sufficient to represent the smallest ice shelves. Following previous statistical downscaling over Greenland [67] or Antarctica [68], we downscale the 35-km outputs to the common 4-km grid. The method consists of a bi-linear interpolation to 4-km, followed by a correction based on the local gradient of the interpolated variable with altitude, defined from the 4 closest neighbours.

Calving flux

There is no parameterisation estimating the evolution of the calving flux without the use of an ice-sheet model and our confidence in existing methods used to parameterise iceberg calving is limited. As a consequence, to include a lower boundary for calving, we set the calving flux to zero in the main study.

Instead of assuming the calving flux to be zero, it can also be assumed that iceberg calving will remain constant or increase in the future, as suggested by previous studies for most scenarios [39, 40]. We investigated the influence of this assumption by reconducting the analysis using calving values from observational estimates [15] instead of fixing it to zero. Extended Data Fig. 6 and 7 were computed using this assumption. This leads to a slightly higher number of non-viable ice shelves by 2300, on the order of 10% for the high-emission scenario, and highlights the role of calving for the mass balance of a range of small ice shelves. It does, however, not substantially alter the main conclusions of our study.

Instead of one ice shelf, two ice shelves become likely non-viable in the low-emission scenario by 2300 (Extended Data Fig. 6). Instead of 26, 32 of them become likely non-viable before 2150 in the high-emission scenario, a number that raises to 44 out of 64

by 2300 (instead of 38) and 33 very likely non-viable ice shelves by 2300 (instead of 30). In the period between approximately 2085 and 2185 50% of the ice shelves reach at least likely non-viability (instead of 44%), and 41% very likely (instead of 30%). The long-term sea-level rise potential is of ∼11 m instead of ∼10 m, when aggregating the volume above flotation of all basins associated with ice shelves that are likely non-viable by 2300.

Including a non-zero calving in the analysis of the drivers of non-viability highlights the relative role of present calving compared to the mass exchange with the atmosphere and the ocean (Extended Data Fig. 7). The ocean is by far the main driver for reaching non-viability, followed to a lower extent by calving, and a much smaller influence of the surface mass balance. The six ice shelves where the ocean is not the main driver are the remains of Larsen B, Conger/Glenzer, Wordie, Ferrigno, and Ninnis ice shelves, where calving prevails. These are ice shelves where calving already is the main contributor to the present-day mass balance [15].

Present calving represents on average 32% and 25% of the mass loss needed to reach non-viability for the low- and high-emission scenarios respectively. As the calving estimate is on the conservative side, a future increase in calving would lead to an earlier date of effective non-viability. Nevertheless, the low relative contribution of calving to non-viability suggests that this would influence this date only by a few years on average.

Grounding-line flux

The mass flux feeding the ice shelf from the grounded ice sheet (hereafter grounding-line flux) is mainly modulated by the buttressing arising from the contact of the ice shelves with ice rises, rumples, and lateral margins. To estimate an upper limit for the grounding-line flux, we therefore estimate the grounding-line flux occurring when no ice shelf is present downstream of the grounding line, the limit between grounded ice

sheet and floating ice shelf. To do so, we conduct simulations similar to the Antarctic BUttressing Model Intercomparison Project (ABUMIP) [69].

We conduct this experiment with the Finite Element ice-sheet and ice flow model Elmer/Ice [70], using the 2D Shallow-Shelf approximation to simulate the ice flow [e.g. 71–73]. We consider the present geometry from BedMachine-v2 [52] and invert for basal friction and ice viscosity parameters that allow for the ice flow model to best match observations of surface velocities [71–73]. This method enables, by construction, the simulated geometry and ice velocity to be as close as possible to present-day observations.

From there, we recompute diagnostic ice flow responses with and without ice shelves as well as the corresponding grounding-line flux. We use the following Weertman friction law:

$$\boldsymbol{\tau}_b = C_m |\boldsymbol{u}|^{1/m-1} \boldsymbol{u} \tag{4}$$

with C_m the friction parameter and $m \in [1 - \infty]$ where increasing values of m are characteristic of a more plastic bed. We first conducted the inversion with $m = 1$ but it has been proven that larger values might be more realistic in some regions like the Amundsen (m = 5 in Gillet-Chaulet et al. [74]). We therefore conduct diagnostic experiments with and without ice shelves accounting for $m = [1, 3, 5]$ (and adjusting for C_m) to assess the sensitivity to the friction law [75]. The impact of the value of m is relatively different basin to basin but our results align well with the sensitivity test of Gudmundsson et al. [75] where they show a grounding line flux about 50-100% higher with $m = 3$ than with $m = 1$. The different bed plasticities are applied on the whole Antarctic ice sheet, giving us three possible grounding-line fluxes for each ice shelf. The weighting process then determines which parameterisation-model-plasticity combinations influence our viability limit most (Extended Data Fig. 12).

Using the BedMachine geometry including the ice shelves results in a reference total grounding-line flux for Antarctica ranging from 1843 to 2124 $\mathrm{Gt\,yr^{-1}}$, depending on the value of m. This value is very close to observations (2048 ± 149 $\mathrm{Gt\,yr^{-1}}$ [65]). This reference flux is multiplied by $\sim$3.5 to $\sim$7 when removing the ice shelves. While the removal of some ice shelves leads to a large increase in grounding-line flux (e.g. Ross, Filchner-Ronne, Amery, Moscow University, Totten), other glaciers initially exhibiting high fluxes do not largely increase them after losing their ice shelves (e.g. Thwaites, Pine Island). This behavior is usually in agreement with the mapping of buttressing potential [3].

Defining non-viability

Non-viability is reached when the ice-shelf mass balance becomes negative at one date and all following ones. In other words, the non-viability limit defined here represents ocean and atmosphere conditions for which it is virtually impossible that an ice shelf maintains its current shape on the long term despite the grounding-line flux being maximal and the calving flux being minimal. The non-viability of an ice shelf in these conditions can therefore be considered as a conservative estimate with regard to ice dynamics. Importantly, we do not attempt to estimate the date at which an ice shelf disintegrates or reaches zero thickness: on the one hand, a slight imbalance can make the ice shelf thin very slowly, and on the other hand, the actual ice flow from the grounded ice sheet would be smaller than in our estimate, making the mass loss faster. Furthermore, as previously mentioned, hydrofracturing, damage and rifting may induce quick collapse of an ice shelf once it has lost enough mass.

We assess the viability of ice shelves with their current extent. If mass loss at the surface and at the base is large enough, an ice shelf will tend to get thinner. This may unpin the ice shelf, increase damage, and overall reduce buttressing, which can in turn increase the ice flow across the grounding line and potentially keep the ice shelf

viable through compensation. As these dynamical effects remain difficult to represent in ice-sheet models, we place ourselves in the extreme case of a maximal ice-shelf mass gain through increased mass flux from the grounded ice sheet, and minimal mass loss through calving.

Our limit of viability represents the ocean and atmosphere conditions for which it is virtually impossible that an ice shelf maintains its current shape on the long term. To confirm that our results remain valid for plausible grounding-line retreat beyond the current ice-sheet geometry, we repeated the analysis on two plausible future ice-sheet geometries, namely for 2100 and 2150, which lie in the period where most ice shelves become likely non-viable (see "Reaching non-viablity") and have therefore the highest potential to influence our conclusions.

The future ice-sheet geometries were simulated using the ice-sheet model Elmer/Ice forced by SSP5-8.5 output from IPSL-CM6A-LR, which is a model with comparably higher climate sensitivity [76] and is thus linked to high SMB [17]. Based on the 2000 geometry (reconstructed from BedMachine and ice thickness rates of change under the hydrostatic hypothesis), and similarly to what has been done for the BedMachine reference flux, the model is initialized by estimating basal sliding and ice viscosity through an inverse modeling approach. This process optimizes these two parameters by minimizing the disparities between modeled and observed surface ice velocities. For this step, we use velocity data from the Making Earth System data records for Use in Research Environments project [MEaSUREs, 77]. This dataset includes a long-term velocity field averaged over the 20 years of satellite data that is usually used as a reference by ice sheet modellers. Annual data, although incomplete, are also available and are used here to infer the 2000 conditions. Because of remaining uncertainties in ice sheet parameters, the inversion often leads to unphysical ice thickness rates of change in some regions. We therefore run a short relaxation (20 years), where the model is allowed to evolve under a constant climate forcing. A simulation is then conducted

from this 2000-like initial state to 2200. During this forward experiments, we use a non-linear Weertman ($m = 3$) sliding law and the basal melt forcing is obtained via the PICO model [61]. We apply the melt on the floating ice but not directly at the grounding line (i.e., melt applied to the first floating node). The reference SMB is given by a RACMOv2.3p2 climatology [78] and an additional anomaly is added based on the SSP5-8.5 IPSL-CM6A-LR climate.

From these simulations, we extract the geometries for the years 2100 and 2150. These new plausible geometries integrate, among others, the effect on the grounding-line flux of (1) a possible increase in snow precipitation on the grounded ice sheet, (2) retreating grounding lines, and (3) ice-shelf thinning. In the same manner as for the original analysis, we remove all ice shelves to infer an upper grounding-line flux estimate for both these geometries and recalculate the surface mass balance and basal mass balance on both these geometries.

The results of this new analysis are shown in Extended Data Fig. 8. Overall, the conclusions are not significantly altered. In both geometries, the number of likely non-viable ice shelves by 2150 (26 in the 2100 geometry and 31 in the 2150 geometry) and by 2300 (43 in the 2100 geometry and 46 in the 2150 geometry) is equal or higher than the numbers inferred for the present geometry in the original analysis. This suggests that our initial estimates are indeed on the conservative side and remain valid even for plausible future geometries.

Regionally, a few differences in the timing of reaching non-viability can be seen compared to the original analysis (compare Extended Data Fig. 8c and d with Fig. 2c in the main text). However, for most of these differences, the likelihood of reaching non-viability increases earlier in time and is sometimes higher by 2300 in the future ice-sheet geometries than in the original analyses (such as for e.g. Pine Island, Thwaites, Dotson, Crosson, but also Moscow University and many others), confirming that our original estimates remain on the conservative side. While for the 2100

ice-sheet geometry the likelihood of non-viability of Amery, Filchner-Ronne and Ross ice shelves is smaller in 2200 and 2300 (only Amery) than in the original analysis, it is comparable or even higher in the 2150 geometry for the same years. The only exception for which the likelihood of non-viability is smaller in 2200 and 2300 than in the original analysis is Cook ice shelf in the 2150 ice-sheet geometry. Overall, these results could indicate that longer grounding lines (induced by grounding-line retreat) and associated grounding-line flux are compensated by increased mass loss at the base and the surface of the ice shelves due to their increased area. This demonstrates that our analysis on the current geometry, combined with our estimate for an upper-bound grounding-line flux, results in robust latest-bounds for non-viability estimates that remain conservative over time.

Constraining the uncertainty

The use of multiple combinations of CMIP6 models, basal melt parameterisations, and bed plasticities gives a large ensemble of possible ice-shelf mass balance evolutions for individual ice shelves. To constrain our analysis to a plausible ensemble for every ice shelf, we weight the different combinations based on the comparison of their historical period to the observational ice-shelf mass balance [15]. To also account for the likelihood of future warming in individual CMIP6 models, these weights are then multiplied by another weight accounting for the plausibility of the model equilibrium climate sensitivity [36, 79]. For information, the distribution of the weights per ice shelf and uncertainty dimension are shown in Extended Data Fig. 10, 11 and 12.

The weight describing the proximity of the historical simulation to observational estimates is inferred using Bayesian calibration similarly to Coulon et al. [40]. For a given ensemble member i (across the model-parameterisation-bed plasticity ensemble),

the score s_i is computed as follows, for each ice-shelf separately:

$$s_i = exp\left(-0.5\frac{(MB_{\text{mod, i}} - MB_{\text{obs}})^2}{\sigma^2_{\text{mod, i}} + \sigma^2_{\text{obs}}}\right) \tag{5}$$

where MB_{mod} and MB_{obs} are the simulated and observational ice-shelf mass balance estimates respectively and σ_{obs} and σ_{mod} are the observational and structural errors. The observational ice-shelf mass balance is calculated from the 1997–2014 mean estimates of Davison et al. [15] for basal mass balance, surface mass balance and grounding-line flux. We use the 1997–2014 mean rather than interannual values because it is considered as a more robust observational estimate. For calving, we use their steady state calving flux rather than their 1997-2014 mean calving flux because this is more consistent with a fixed calving front given that we assess the viability of ice shelves in their current shape, while the actual 1997–2014 calving flux is largely associated with changes in ice-shelf area. The observational uncertainty σ_{obs} is the time-average of the square root of the sum of the squared uncertainties provided by Davison et al. [15] for individual mass fluxes. The structural error σ_{mod} is estimated by taking the standard deviation over time and averaging it across the model-parameterisation-bed plasticity space. From the score, we can then infer a normalised weight, by dividing each s_i by the sum of s_i across the ensemble. Finally, we set the weight to zero if the calving estimate surpasses the maximum estimate of the grounding-line flux as this would mean that the ice shelf is not viable even without basal melt, which is not realistic.

The weight describing the plausibility of the equilibrium climate sensitivity of each climate model is taken from Jourdain et al. [36]. These weights represent the probability, for a given climate model, of a skew-normal distribution fitted to obtain the 5^{th}, 50^{th} and 95^{th} percentiles at an equilibrium climate sensitivity of 2.0, 3.0 and 5.0°C, as expected from multiple lines of evidence [79].

All metrics presented in this study take the resulting weights into account. In particular, we take these weights into account when estimating the likelihood of reaching non-viability, using the definitions commonly used in the IPCC reports [80]: very unlikely, unlikely, as likely as not, likely, and very likely (respectively 0-10%, 10-33%, 33-66%, 66-90%, 90-100% weighted probability across the large ensemble of reaching non-viability).

Supplementary information. Correspondence and requests for materials should be addressed to clara.burgard@locean.ipsl.fr.

Acknowledgements. Most of the computations presented in this paper were performed using the GRICAD infrastructure (https://gricad.univ-grenoble-alpes.fr), which is supported by Grenoble research communities. The NEMO simulations were performed using HPC resources from GENCI–TGCC (MISOCS project, allocation A0140106035). The ocean data processing and emulation of MAR simulations were performed on the IPSL Data and Computing Center (ESPRI). This research was funded by the DEEP-MELT project (IRGA Pack IA 2021-2022) supported by MIAI @ Grenoble Alpes (ANR-19-P3IA-0003), by the European Union's Horizon 2020 research and innovation programme under grant agreements no. 869304 (PROTECT), 101003826 (CRiceS), 821001 (SO-CHIC), by the European Union's Horizon Europe research and innovation programme under grant agreement no. 101081193 (OptimESM) and 101060452 (OCEAN:ICE), as well as by Agence Nationale de la Recherche (ANR) - France 2030 as part of the PEPR TRACCS programme under grant number ANR-22-EXTR-0008 and ANR-22-EXTR-0010, and by ANR through the AIAI project (ANR-22-CE01-0014).

Declarations

Funding

This research was funded by the DEEP-MELT project (IRGA Pack IA 2021-2022) supported by MIAI @ Grenoble Alpes (ANR-19-P3IA-0003), by the European Union's Horizon 2020 research and innovation programme under grant agreements no. 869304 (PROTECT), 101003826 (CRiceS), 821001 (SO-CHIC), by the European Union's Horizon Europe research and innovation programme under grant agreement no. 101081193 (OptimESM) and 101060452 (OCEAN:ICE), as well as by Agence Nationale de la Recherche (ANR) - France 2030 as part of the PEPR TRACCS programme under grant number ANR-22-EXTR-0008 and ANR-22-EXTR-0010, and by ANR through the AIAI project (ANR-22-CE01-0014).

Competing interests

The authors declare no competing interests.

Ethics approval and consent to participate

Not applicable.

Consent for publication

Not applicable.

Data and materials availability

The data used to make the analysis and produce the figures can be found here: https://doi.org/10.5281/zenodo.13768758 [81]. The Antarctic maps in the figures are created using the cartopy package version 0.21.1 in python.

Code availability

The code to extrapolate the CMIP6 data to the stereographic grid can be found here: https://zenodo.org/records/12755910 [53]. All other code used to produce the analysis and the figures is available on the same Zenodo repository as the data: https://doi.org/10.5281/zenodo.13768758 [81].

Author contribution

CB and NCJ developed the original idea of this paper. CK carried out the MAR simulations and part of the NEMO simulations used for the calibration of the basal melt parameterisations. NCJ carried out the MAR emulations and processed the CMIP6 ocean outputs. PM carried out most of the NEMO simulations used for training. CM and JC carried out the present-day ice-sheet simulations and CM carried out the long-term future ice-sheet simulations and the ABUMIP-type experiments. CB calibrated and applied the basal melt parameterisations. CB carried out all analyses and wrote the manuscript. CB, NCJ, CK, CM, PM, JC all contributed to discussions on the design of the study, the analyses and the writing. The authors declare no competing interests. Correspondence and requests for materials should be addressed to clara.burgard@locean.ipsl.fr.

References

[1] Doake, C. S. M., Corr, H. F. J., Rott, H., Skvarca, P. & Young, N. W. Breakup and conditions for stability of the northern Larsen Ice Shelf, Antarctica. *Nature* **391**, 778–780 (1998).

[2] Reese, R., Gudmundsson, G. H., Levermann, A. & Winkelmann, R. The far reach of ice-shelf thinning in Antarctica. *Nat. Clim. Change* **8**, 53–57 (2018).

[3] Fürst, J. *et al.* The safety band of antarctic ice shelves. *Nat. Clim. Change* **6**, 479–482 (2016).

[4] Fox-Kemper, B. *et al. Ocean, Cryosphere and Sea Level Change. Climate Change 2021: The Physical Science Basis. Contribution of Working Group I to the Sixth Assessment Report of the Intergovernmental Panel on Climate Change* (Cambridge University Press, Cambridge, United Kingdom and New York, NY, USA, 2021).

[5] Rignot, E. *et al.* Accelerated ice discharge from the Antarctic Peninsula following the collapse of Larsen B ice shelf. *Geophys. Res. Lett.* **31**, L18401 (2004).

[6] Scambos, T. A., Bohlander, J. A., Shuman, C. A. & Skvarca, P. Glacier acceleration and thinning after ice shelf collapse in the Larsen B embayment, Antarctica. *Geophys. Res. Lett.* **31** (2004).

[7] Robin, G. d. Q. & Adie, R. J. *The Ice Cover*, 100–117 (Butterworths, London, 1964).

[8] Mercer, J. H. West Antarctic ice sheet and CO2 greenhouse effect: a threat of disaster. *Nature* **271**, 321–325 (1978).

[9] Vaughan, D. & Doake, C. Recent atmospheric warming and retreat of ice shelves on the Antarctic Peninsula. *Nature* **379**, 328–331 (1996).

[10] Cook, A. & Vaughan, D. Overview of areal changes of the ice shelves on the Antarctic Peninsula over the past 50 years. *Cryosphere* **4**, 77–98 (2010).

[11] Weertman, J. Stability of the Junction of an Ice Sheet and an Ice Shelf. *J. Glaciol.* **13**, 3–11 (1974).

[12] Schoof, C. Ice sheet grounding line dynamics: Steady states, stability, and hysteresis. *J. Geophys. Res.* **112**, F03S28 (2007).

[13] DeConto, R. & Pollard, D. Contribution of Antarctica to past and future sea-level rise. *Nature* **531**, 591–597 (2016).

[14] Bassis, J. N. *et al.* Stability of ice shelves and ice cliffs in a changing climate. *Annu. Rev. Earth Planet. Sci.* **52** (2024).

[15] Davison, B. *et al.* Annual mass budget of Antarctic ice shelves from 1997 to 2021. *Sci. Adv.* **9**, eadi0186 (2023).

[16] Paolo, F., Fricker, H. & Padman, L. Volume loss from Antarctic ice shelves is accelerating. *Science* **348**, 327–331 (2015).

[17] Kittel, C. *et al.* Diverging future surface mass balance between the Antarctic ice shelves and grounded ice sheet. *Cryosphere* **15**, 1215–1236 (2021).

[18] van Wessem, J. M., van den Broeke, M. R., Wouters, B. & Lhermitte, S. Variable temperature thresholds of melt pond formation on antarctic ice shelves. *Nat. Clim. Change* **13**, 161–166 (2023).

[19] Timmermann, R. & Hellmer, H. H. Southern Ocean warming and increased ice shelf basal melting in the twenty-first and twenty-second centuries based on coupled ice-ocean finite-element modelling. *Ocean Dyn.* **63**, 1011–1026 (2013).

[20] Mathiot, P. & Jourdain, N. Southern Ocean warming and Antarctic ice shelf melting in conditions plausible by late 23rd century in a high-end scenario. *Ocean Sci.* **19**, 1595–1615 (2023).

[21] Scambos, T. A., Hulbe, C., Fahnestock, M. & Bohlander, J. The link between climate warming and break-up of ice shelves in the Antarctic Peninsula. *J. Glaciol.*

46, 516–530 (2000).

[22] Scambos, T., Hulbe, C. & Fahnestock, M. *Climate-Induced Ice Shelf Disintegration in the Antarctic Peninsula*, 79–92 (American Geophysical Union (AGU), 2003).

[23] Skvarca, P., De Angelis, H. & Zakrajsek, A. F. Climatic conditions, mass balance and dynamics of Larsen B ice shelf, Antarctic Peninsula, prior to collapse. *Ann. Glaciol.* **39**, 557–562 (2004).

[24] Lai, C.-Y. *et al.* Vulnerability of Antarctica's ice shelves to meltwater-driven fracture. *Nature* **584**, 574–578 (2020).

[25] Shepherd, A., Wingham, D., Payne, T. & Skvarca, P. Larsen ice shelf has progressively thinned. *Science* **302**, 856–859 (2003).

[26] Lhermitte, S., Wouters, B. & HiRISE Team. *The triggers for Conger Ice Shelf demise: Long-term weakening vs. short-term collapse*, EGU–16400 (2023).

[27] Walker, C. *et al.* The Multi-decadal Collapse of East Antarctica's Conger-Glenzer Ice Shelf. *Nature Geoscience* **17**, 1240–1248 (2024).

[28] Wild, C. T. *et al.* Weakening of the pinning point buttressing Thwaites Glacier, West Antarctica. *Cryosphere* **16**, 397–417 (2022).

[29] Lenaerts, J. T. M. *et al.* Climate and surface mass balance of coastal West Antarctica resolved by regional climate modelling. *Ann. Glaciol.* **59**, 29–41 (2018).

[30] Donat-Magnin, M. *et al.* Future surface mass balance and surface melt in the Amundsen sector of the West Antarctic Ice Sheet. *Cryosphere* **15**, 571–593 (2021).

[31] Rignot, E., Vaughan, D. G., Schmeltz, M., Dupont, T. & MacAyeal, D. Acceleration of Pine island and Thwaites glaciers, west Antarctica. *Ann. Glaciol.* **34**, 189–194 (2002).

[32] Rignot, E., Mouginot, J., Morlighem, M., Seroussi, H. & Scheuchl, B. Widespread, rapid grounding line retreat of Pine Island, Thwaites, Smith, and Kohler glaciers, West Antarctica, from 1992 to 2011. *Geophys. Res. Lett.* **41**, 3502–3509 (2014).

[33] Lhermitte, S. *et al.* Damage accelerates ice shelf instability and mass loss in Amundsen Sea Embayment. *Proc. Natl. Acad. Sci. U.S.A.* **117**, 24735–24741 (2020).

[34] Seroussi, H. *et al.* Insights into the vulnerability of Antarctic glaciers from the ISMIP6 ice sheet model ensemble and associated uncertainty. *Cryosphere* **17**, 5197–5217 (2023).

[35] Eyring, V. *et al.* Overview of the Coupled Model Intercomparison Project Phase 6 (CMIP6) experimental design and organization. *Geosci. Model Dev.* **9**, 1937–1958 (2016).

[36] Jourdain, N., Amory, C., Kittel, C. & Durand, G. Changes in Antarctic surface conditions and potential for ice shelf hydrofracturing from 1850 to 2200. *The Cryosphere* 1641—-1674 (2025).

[37] Burgard, C., Jourdain, N., Reese, R., Jenkins, A. & Mathiot, P. An assessment of basal melt parameterisations for Antarctic ice shelves. *Cryosphere* **16**, 4931–4975 (2022).

[38] Burgard, C. *et al.* Emulating Present and Future Simulations of Melt Rates at the Base of Antarctic Ice Shelves With Neural Networks. *J. Adv. Model. Earth*

Syst. **15**, e2023MS003829 (2023).

[39] Park, J.-Y. *et al.* Future sea-level projections with a coupled atmosphere-ocean-ice-sheet model. *Nat. Commun.* **14**, 636 (2023).

[40] Coulon, V. *et al.* Disentangling the drivers of future Antarctic ice loss with a historically calibrated ice-sheet model. *Cryosphere* **18**, 653–681 (2024).

[41] Morlighem, M. *et al.* The West Antarctic Ice Sheet may not be vulnerable to marine ice cliff instability during the 21st century. *Science Advances* **10**, eado7794 (2024).

[42] Morris, E. M. & Vaughan, D. G. *Spatial and Temporal Variation of Surface Temperature on the Antarctic Peninsula And The Limit of Viability of Ice Shelves*, 61–68 (American Geophysical Union (AGU), 2003).

[43] Benn, D. *et al.* Rapid fragmentation of Thwaites Eastern Ice Shelf. *The Cryosphere* **16**, 2545–2564 (2022).

[44] Wild, C. *et al.* Rift propagation signals the last act of the Thwaites Eastern Ice Shelf despite low basal melt rates. *Journal of Glaciology* **70**, e21 (2024).

[45] De Rydt, J. & Naughten, K. Geometric amplification and suppression of ice-shelf basal melt in West Antarctica. *Cryosphere* **18**, 1863–1888 (2024).

[46] Bradley, A. T., Bett, D. T., Dutrieux, P., De Rydt, J. & Holland, P. R. The Influence of Pine Island Ice Shelf Calving on Basal Melting. *J. Geophys. Res.* **127**, e2022JC018621 (2022).

[47] Beadling, R. *et al.* Representation of Southern Ocean Properties across Coupled Model Intercomparison Project Generations: CMIP3 to CMIP6. *J. Clim.* **33**, 6555–6581 (2020).

[48] Heuzé, C. Antarctic Bottom Water and North Atlantic Deep Water in CMIP6 models. *Ocean Sci.* **17**, 59–90 (2021).

[49] Smith, R. *et al.* Coupling the U.K. Earth System Model to Dynamic Models of the Greenland and Antarctic Ice Sheets. *J. Adv. Model. Earth Syst.* **13**, e2021MS002520 (2021).

[50] Martin, D. F., Cornford, S. L. & Payne, A. J. Millennial-Scale Vulnerability of the Antarctic Ice Sheet to Regional Ice Shelf Collapse. *Geophys. Res. Lett.* **46**, 1467–1475 (2019).

[51] Rignot, E. *et al.* Four decades of Antarctic Ice Sheet mass balance from 1979–2017. *Proc. Natl. Acad. Sci. U.S.A.* **116**, 1095–1103 (2019).

[52] Morlighem, M. MEaSUREs BedMachine Antarctica, Version 2. (2020). Boulder, Colorado USA. NASA National Snow and Ice Data Center Distributed Active Archive Center.

[53] Jourdain, N. C. nicojourdain/CMIP6_data_to_ISMIP6_grid: v1.0 (v1.0). Tech. Rep., Zenodo (2024). URL https://doi.org/10.5281/zenodo.12755910.

[54] Jourdain, N. *et al.* A protocol for calculating basal melt rates in the ISMIP6 Antarctic ice sheet projections. *Cryosphere* **14**, 3111–3134 (2020).

[55] Beckmann, A. & Goosse, H. A parameterization of ice shelf–ocean interaction for climate models. *Ocean Model.* **5**, 157–170 (2003).

[56] Holland, P., Jenkins, A. & Holland, D. The Response of Ice Shelf Basal Melting to Variations in Ocean Temperature. *J. Clim.* **21**, 2558–2572 (2008).

[57] Little, C. M., Gnanadesikan, A. & Oppenheimer, M. How ice shelf morphology controls basal melting. *J. Geophys. Res.* **114** (2009).

[58] Jenkins, A. *et al.* West Antarctic Ice Sheet retreat in the Amundsen Sea driven by decadal oceanic variability. *Nat. Geosci.* **11**, 733–738 (2018).

[59] Lazeroms, W., Jenkins, A., Gudmunsson, G. & van de Wal, R. Modelling present-day basal melt rates for Antarctic ice shelves using a parametrization of buoyant meltwater plumes. *Cryosphere* **12**, 49–70 (2018).

[60] Lazeroms, W., Jenkins, A., Rienstra, S. & van de Wal, R. An Analytical Derivation of Ice-Shelf Basal Melt Based on the Dynamics of Meltwater Plumes. *J. Phys. Oceanogr.* **49**, 917–939 (2019).

[61] Reese, R., Albrecht, T., Mengel, M., Asay-Davis, X. & Winkelmann, R. Antarctic sub-shelf melt rates via PICO. *Cryosphere* **12**, 1969–1985 (2018).

[62] Lambert, E. & Burgard, C. Brief communication: Sensitivity of Antarctic ice shelf melting to ocean warming across basal melt models. *The Cryosphere* **19**, 2495–2505 (2025).

[63] NEMO Team. NEMO ocean engine. *Scientific Notes of Climate Modelling Center* **27** (2019).

[64] Tsujino, H. *et al.* JRA-55 based surface dataset for driving ocean–sea-ice models (JRA55-do). *Ocean Model.* **130**, 79–139 (2018).

[65] Rignot, E., Jacobs, S., Mouginot, J. & Scheuchl, B. Ice-shelf melting around Antarctica. *Science* **341**, 266–270 (2013).

[66] Gallée, H. & Schayes, G. Development of a three-dimensional meso-γ primitive equation model: katabatic winds simulation in the area of Terra Nova Bay, Antarctica. *Mon. Weather Rev.* **122**, 671–685 (1994).

[67] Franco, B., Fettweis, X., Lang, C. & Erpicum, M. Impact of spatial resolution on the modelling of the Greenland ice sheet surface mass balance between 1990–2010, using the regional climate model MAR. *Cryosphere* **6**, 695–711 (2012).

[68] Noël, B. *et al.* Higher Antarctic ice sheet accumulation and surface melt rates revealed at 2 km resolution. *Nat. Commun.* **14**, 7949 (2023).

[69] Sun, S. *et al.* Antarctic ice sheet response to sudden and sustained ice-shelf collapse (ABUMIP). *J. Glaciol.* **66**, 891–904 (2020).

[70] Gagliardini, O. *et al.* Capabilities and performance of Elmer/Ice, a new-generation ice sheet model. *Geosci. Model Dev.* **6**, 1299–1318 (2013).

[71] Brondex, J., Gillet-Chaulet, F. & Gagliardini, O. Sensitivity of centennial mass loss projections of the Amundsen basin to the friction law. *Cryosphere* **13**, 177–195 (2019).

[72] Klein, E. *et al.* Annual cycle in flow of Ross Ice Shelf, Antarctica: contribution of variable basal melting. *J. Glaciol.* **66**, 861–875 (2020).

[73] Mosbeux, C., Padman, L., Klein, E., Bromirski, P. & Fricker, H. Seasonal variability in Antarctic ice shelf velocities forced by sea surface height variations. *Cryosphere* **17**, 2585–2606 (2023).

[74] Gillet-Chaulet, F. *et al.* Assimilation of surface velocities acquired between 1996 and 2010 to constrain the form of the basal friction law under Pine Island Glacier. *Geophys. Res. Lett.* **43**, 10,311–10,321 (2016).

[75] Gudmundsson, G. H., Paolo, F. S., Adusumilli, S. & Fricker, H. Instantaneous Antarctic ice sheet mass loss driven by thinning ice shelves. *Geophys. Res. Lett.* **46**, 13903–13909 (2019).

[76] Meehl, G. *et al.* Context for interpreting equilibrium climate sensitivity and transient climate response from the CMIP6 Earth system models. *Science Advances* **6**, eaba1981 (2020).

[77] Rignot, E., Mouginot, J. & Scheuchl, B. MEaSUREs InSAR-based Antarctica Ice Velocity map, Version 2. (2017). Boulder, Colorado USA. NASA National Snow and Ice Data Center Distributed Active Archive Center.

[78] van Wessem, J. M. *et al.* Modelling the climate and surface mass balance of polar ice sheets using RACMO2 – Part 2: Antarctica (1979–2016). *The Cryosphere* **12**, 1479–1498 (2018).

[79] Forster, P. *et al.* in *The Earth's energy budget, climate feedbacks, and climate sensitivity. Climate Change 2021: The Physical Science Basis. Contribution of Working Group I to the Sixth Assessment Report of the Intergovernmental Panel on Climate Change* (eds Masson-Delmotte, V. *et al.*) 923–1054 (Cambridge, United Kingdom and New York, NY, USA, 2021).

[80] Mastrandrea, M. *et al.* Guidance Note for Lead Authors of the IPCC Fifth Assessment Report on Consistent Treatment of Uncertainties. *Intergovernmental Panel on Climate Change (IPCC)* (2010). URL http://www.ipcc.ch.

[81] Burgard, C. *et al.* Data and scripts to reproduce figures from "Ocean warming threatens the viability of 60% of Antarctic ice shelves". Tech. Rep., Zenodo (2025). URL https://doi.org/10.5281/zenodo.13768758.